

Determining Spectroscopic Redshifts by Using k Nearest Neighbors Regression

I. Description of Method and Analysis

S. D. Kügler¹, K. Polsterer¹, and M. Hoecker¹

Heidelberger Institut für Theoretische Studien (HITS), Schloss-Wolfsbrunnenweg 35, D-69118 Heidelberg, Germany
email: dennis.kuegler@h-its.org

Received/Accepted

Abstract

Context. In astronomy, new approaches to process and analyze the exponentially increasing amount of data are inevitable. For spectra, such as in the Sloan Digital Sky Survey spectral database, usually templates of well-known classes are used for classification. In case the fitting of a template fails, wrong spectral properties (e.g. redshift) are derived. Validation of the derived properties is the key to understand the caveats of the template-based method.

Aims. In this paper we present a method to statistically compute the redshift z based on a similarity approach. This allows us to determine redshifts in spectra for emission and absorption features without using any predefined model. Additionally we show how to determine the redshift based on single features. As a consequence we are, e.g. able to filter objects which show multiple redshift components.

Methods. The redshift calculation is performed by comparing predefined regions in the spectra and applying a nearest neighbor regression model for every predefined emission and absorption region, individually.

Results. The choice of the model parameters controls the quality and the completeness of the redshifts. For $\approx 90\%$ of the analyzed 16,000 spectra of our reference and test sample a certain redshift can be computed which is comparable to the completeness of SDSS (96%). The redshift calculation yields a precision for every individually tested feature that is comparable with the overall precision of the redshifts of SDSS. Using the new method to compute redshifts we could additionally identify 14 spectra with a significant shift between emission and absorption or emission and emission lines. The results show already the immense power of this simple machine learning approach for investigating huge databases such as the SDSS.

Key words. Galaxies: distances and redshifts – Astronomical data bases – Catalogs – Methods: data analysis – Methods: statistical

1. Introduction

In the past decades the rapidly increasing amount of available data has been one of the greatest challenges in astronomy. In contrast to the amount of data, the number of techniques and the knowledge how to analyze these large data sets increased only slowly over time. When the first digital, photometric all-sky surveys were performed, the amount of available data was already too large to be inspected manually. With the advent of spectroscopic surveys and additional photometric surveys in multiple wavelengths, the available data volume increased so rapidly that novel approaches are mandatory.

So far the most successful survey in astronomy is the Sloan Digital Sky Survey (SDSS, York et al. 2000) which contains in its current 10th data release (DR10, Ahn et al. 2014) photometry for one billion objects and spectra covering the near-UV to the near-IR for roughly three million objects. In future, surveys such as the Large Sky Area Multi-Object Fiber Spectroscopic Telescope (LAMOST, Cui et al. 2012) will reach this amount of data in a fraction of the time needed by SDSS. Thus more advanced techniques for handling those immense data streams have to be developed.

The determination of spectral redshifts and classifications of the SDSS spectra is based on template fitting. Therefore generalized templates are created by combining spectra of similar objects for all empirically determined classes of objects. By fitting

those templates to the spectra, a number of predefined properties, e.g. redshift, can be individually computed for every object. By applying all available templates to the data while allowing for some variation in a set of parameters, e.g. width of features, and testing the reliability of every model by computing a reduced χ^2 , the best fitting template is determined. Instead of using the full information available, just a simplified model with a limited flexibility is applied which does not allow a more detailed discussion of individual properties. Furthermore the choice of the reference spectra and the creation of these templates has a strong impact on the determined properties.

With this publication we want to emphasize the power of statistical learning in huge spectral databases. Hereby, huge refers to a large number of entities and dimensions. While this approach can principally be applied to any database, we focus on SDSS. There are many applications of machine learning techniques in astronomy (see Borne 2009; Ball & Brunner 2010). So far spectroscopically derived properties have been mainly used as ground truth to, e.g. estimate redshifts on photometric data (see Laurino et al. 2011; Gieseke et al. 2011; Polsterer et al. 2013). In contrast less attention has been paid to the application of machine learning to the spectral data itself (see Richards et al. 2009; Meusinger et al. 2012) which can be mainly attributed to the “curse of dimensionality” (see Bellman & Bellman 1961). The ultimate goal would be to obtain spectral properties which

are not based on the created templates but on the rich experience existing in the database instead.

The algorithm presented in this paper will perform a consistency check of the redshift calculated by the SDSS pipeline. We therefore assume that the majority of the spectra is fairly well described by one of the templates and thus the redshift is determined reasonably precise. Of course the templates do not describe all kinds of objects perfectly, thus at least some will be misfit. The great improvement in calculating redshifts based on a data-driven approach is that the redshifts can be determined model-independent. This method is suitable for determining redshifts of unknown spectra and in a forth-coming paper we will present a value-added catalog of redshifts to the existing SDSS spectra. In this paper we will focus on the technical side and explain the impact of the choice of different model parameters. In order to highlight the power of this new method, some outliers in terms of redshift in the used subsample are presented. The motivation for employing new methods for redshift computation is manifold:

1. *Validation*: Cross-validating the self-consistency of the computed redshifts is crucial to understand caveats of the SDSS pipeline. The independent determination of a redshift increases the confidence and the number of reliable redshifts.
2. *Calculating redshifts*: We are able to determine model-independent redshifts of existing and future spectra with high precision. This is possible since we are determining the redshift as an ensemble property and thus the theoretical resolution can be improved statistically with the number of similar spectra in the reference database as well as with the dimension of the feature vector.
3. *Rare objects*: Many different attempts have been performed to find rare objects in the SDSS spectral database which show shifts between spectral features (see Bolton et al. 2004; Tsalmantza et al. 2011). With the presented method we will be able to detect more of those since our method can deal with lower S/N than the template fits.
4. *Unexpected behavior*: This can be caused by objects of a previously unknown class or by a superposition of two classes. Those objects might possibly be the science drivers in the near future. Also artifacts in the reduction pipeline/in the data can be discovered.

The paper is structured as follows: §2 describes the data used for creating and testing our model. In §3 we will explain the basic approach used in our method in more detail. In §4 we discuss the performance of our method in terms of precision and reliability. Also some outliers and peculiar objects are discussed in more detail. A summary and an outlook will follow in §5. In a follow-up paper we describe the value-added catalog which gives redshifts for all available objects based on specific spectral regions. Additionally a catalog containing all detected outliers will be presented there.

2. The SDSS Spectroscopic Database

For testing our method we are analyzing the spectroscopic database of SDSS. This survey uses a dedicated 2.5m mirror telescope located at the Apache Point Observatory (New Mexico, USA) to map the northern galactic cap and is a joint project by USA, Japan, Korea and Germany.

The telescope was first used to image different stripes of the northern hemisphere in 5 filter bands using the drift scan method. Subsequently interesting objects were selected by brightness limits and different colors cuts for spectroscopy ($R = \lambda/\Delta\lambda \approx 2,000$) with $3,600 \text{ \AA} \leq \lambda \leq 10,000 \text{ \AA}$ (Eisenstein et al. 2001; Richards et al. 2002; Strauss et al. 2002). Note that those selection criteria directly have an impact on the quality of reference sample. In the current DR10 (Ahn et al. 2014) more than 3 million spectra were taken of which far more than 2 million are non-stellar sources according to the SDSS-classification.

It is important to mention that depending on the applied learning technique a large number of reference objects with a representative sampling is mandatory. With millions of objects, the SDSS is more than sufficiently large.¹

2.1. Data Calibration/SDSS pipeline

As mentioned in the caveats of SDSS, the night sky subtraction can suffer from severe inaccuracy by rapidly changing conditions, e.g. auroral activity. Thus the night sky subtraction leaves a severe signature in some of the spectra, which is sometimes not taken into account correctly in the error estimation. As a consequence faint features in the vicinity of strong night sky emission lines might be artifacts. The spectra are automatically labeled, flux as well as wavelength calibrated, and eventually combined with potentially pre-existing observed spectra of the same object.

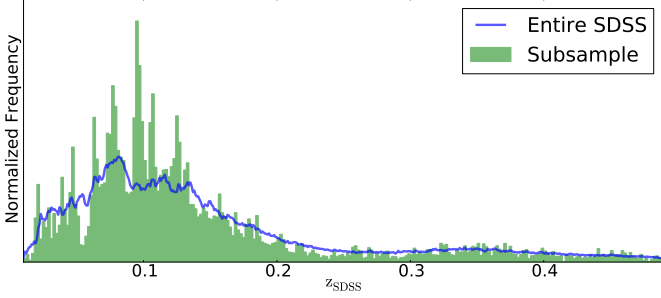
In a second step the calibrated spectra were processed via an identification pipeline which assigned a redshift, a classification and a velocity dispersion to the individual spectra (Bolton et al. 2012). The classification and redshift determination was hereby performed with a principal component analysis (PCA) of a rest-frame shifted training sample. A linear combination of eigenspectra were then shifted with respect to flux and wavelength until a minimal residual was reached. The precision of the redshift for a single line is limited by the resolution per pixel ($\sim 100 \text{ km s}^{-1}$) of the spectrograph but can be improved by computing it independently for all lines available. This method is extremely efficient for spectra which show the expected behavior and as confirmed by performing a self-consistency check later on, the quality of the SDSS redshifts has a high reliability.

2.2. Reference And Test Sample

The analysis of the method was performed on a small subsample of the SDSS data in order to make the different model and parameter evaluations computationally feasible. The analysis of the algorithm is limited to the plates 0266 to 0289 including the exposures of all modified Julian dates (MJDs). Additionally the sample was restricted to the redshift range between $0.01 \leq z \leq 0.5$. The selected restriction allows a more reliable prediction of the regression value, as the density of reference targets in the direct neighborhood is sufficiently high. The chosen subsample includes 16,049 spectra in total. The redshift distribution of the spectra can be found in Figure 1. In the following, this sample will be used as reference and test set at the same time, i.e. we will perform a leave-one-out cross validation. That means that all but

¹ This statement is not only valid for the in-sample method presented here but also for the application on other datasets, **as long as the wavelength coverage and the target selection criteria are comparable**. This is because the data complexity of the reference sample, SDSS in this case, remains the same and thus a comparable number of references is needed for a similar precision.

Figure 1: Comparison of the redshift distribution of the selected subsample (green) and the entire SDSS (blue). Note a steep drop in the frequency towards redshifts $z > 0.25$. Single redshift bins are apparently undersampled.



the target spectrum are reference spectra. As we are only able to compute redshifts within the covered feature space, under-represented objects (high-redshifted galaxies, QSO) will yield worse redshifts than normally represented redshifts.

3. Applied Method

The basic idea for determining the spectroscopic redshift z is to perform a comparison between similar objects. This is done by finding objects which look similar in terms of Euclidean distance and then computing the regression value of the unknown target by comparing it to the redshifts of the most similar spectra.

To be able to compare the spectra, instead of using the plain SDSS spectra we have to pre-process them.

The method is a purely data-driven approach without deriving a generalization and thus the quality of the redshifts relies directly on the chosen reference sample. While this seems contradictory on first sight the method performs comparably on a smaller but representative reference set. It is obvious that the choice of a representative reference sample can just be obtained when domain-knowledge is included. Limiting the reference sample in redshift space would limit the derived values, respectively.

3.1. k Nearest Neighbors (k NN) Regression

Our method is based on k nearest neighbor (k NN) regression which is a commonly used technique in statistical learning (Hastie et al. 2009). All spectra have d datapoints (corresponding to the individual flux measurements in the spectra) and are thus members of a d -dimensional feature space. The reference sample \mathcal{R} consists of m entities which corresponds to the number of reference spectra from which the model learns, 16,048 in this case. Mathematically this sample can be described with,

$$\mathcal{R} = ((\bar{x}_1, y_1), \dots, (\bar{x}_m, y_m)) \in \mathbb{R}^d \times \mathbb{R} \quad (1)$$

where \bar{x}_i is the i -th d -dimensional input vector (spectrum under consideration) corresponding to the flux value in each pixel and y_i is the redshift value z assigned by the SDSS pipeline.

The k NN regression is based on calculating similarities in the d -dimensional feature space. For any d -dimensional feature vector \bar{s} the similarity to a reference object \bar{x}_i can be estimated with distance measure $\Delta(\bar{x}_i, \bar{s})$. The most commonly used met-

rics are:

$$\Delta(\bar{x}_i, \bar{s}) = \left(\sum_{j=1}^d |\bar{x}_{ij} - \bar{s}_j|^p \right)^{1/p} := \begin{cases} \text{Manhattan} & \text{for } p = 1 \\ \text{Euclidean} & \text{for } p = 2 \\ \text{Minkowski} & \text{otherwise} \end{cases}$$

The impact of the choice of the metric on the final results was only marginal. Therefore we solely use the common Euclidean distance. In general the neighbourhood $N_k(\bar{s})$ is determined on the basis of the representation of the reference objects \bar{x}_i in the feature space, such that

$$y(\bar{s}) = \frac{1}{k} \sum_{\bar{x}_i \in N_k(\bar{s})} y_i = \text{mean}_{\bar{x}_i \in N_k(\bar{s})}(y_i) \quad (2)$$

however here we make use of a modified version:

$$y(\bar{s}) = \text{median}_{\bar{x}_i \in N_k(\bar{s})}(y_i) \quad (3)$$

For finding the k most similar spectra $N_k(\bar{s})$ different algorithms exist. The most straight-forward one being the brute-force method where simply every spectrum is compared to each other and the distance is computed. In contrast, spatial structures exist (kd-, ball-trees) which are able to structure the data in advance. Thereby the average time to find the closest spectra is significantly lower once the search structure is created. When experimenting with spatial trees we learned that apparently the dimension of our data is so high and the data themselves are so unstructured that spatial trees do not perform significantly better than the brute-force method and as a consequence only the brute force method is used throughout the paper and for the future catalog.

The considered k NN regression is limited to interpolation of values within the reference sample. As a consequence redshifts of objects with extremely high redshift or very peculiar spectral features can not be determined correctly.

3.2. Requirements

The method of k NN regression can only work efficiently if the following requirements are met:

1. The majority of redshift determinations by SDSS is correct:

In the following the deviation of the SDSS redshifts in comparison to the correct redshift is assumed to be small. This is verified by comparing our results to the redshifts determined by SDSS. One has to keep in mind that for a large fraction of the data the template fitting works quite well and the redshifts are fairly reliable.
2. The number of objects in the reference data set is large compared to the dimensionality:

This is already met in our test sub-sample. Nonetheless this is quite surprising as the number of entities is in the order of the number of dimensions (4,000). It appears that the multi-dimensional feature space is sufficiently homogeneously populated with reference objects. Applying this method to the entire database will just strengthen that assumption further.

- It is possible to distinguish noise from real signals for most of the data:

This requirement is harder to meet as the distinction between signals and noise, especially for low S/N spectral lines, has always been a huge challenge for astronomers. In this work we will use an approach that is based on a simple similarity measure used by the type of the applied regression method. The basic assumption is: When a detectable line exists anywhere in the spectrum it should be possible to find similar spectra which, within their errors, have a similar redshift. Those form a sharp distribution around the real value. On the other hand a spectrum that contains pure noise will yield an even distribution of redshift values over the entire tested redshift range and thus the average deviation from the median/mean will be quite high. In the distribution of so called errors, which correspond to the deviation of reference redshifts across similar spectra, one would naively expect a superposition of two behaviors: The dominant component is a distribution which shows a drop towards higher deviations with a width that is comparable to the sensitivity of the method. This distribution corresponds to redshifts based on true absorption/emission lines. Underlying to the first component there is a flatter distribution representing the spectra which contain mostly noise. This will be further discussed in Section 4.

3.3. Pre-processing

The pre-processing is needed to make the spectra comparable. Effects like apparent brightness are not important, since we are solely interested in absorption and emission features. Therefore the behavior of the continuum has to be estimated and subtracted.

3.3.1. Regridding

The dispersion resolution between different fibers on a single plate and between the plates themselves differ slightly. In order to always be able to compare the correct wavelength bins, which do not exactly agree with redshift bins, the spectra have to be re-gridded. We are therefore creating a global grid which is defined by:

$$\log(\lambda(p)) = 0.0001 \cdot p + 3.5222 \quad (4)$$

where λ is the wavelength in \AA for a given pixel position p , with $0 \leq p < 5,100$. The parameters of the function are chosen such that the dispersion solution corresponds to the average of our selected subsample. The regridding is performed such that the total flux is conserved.

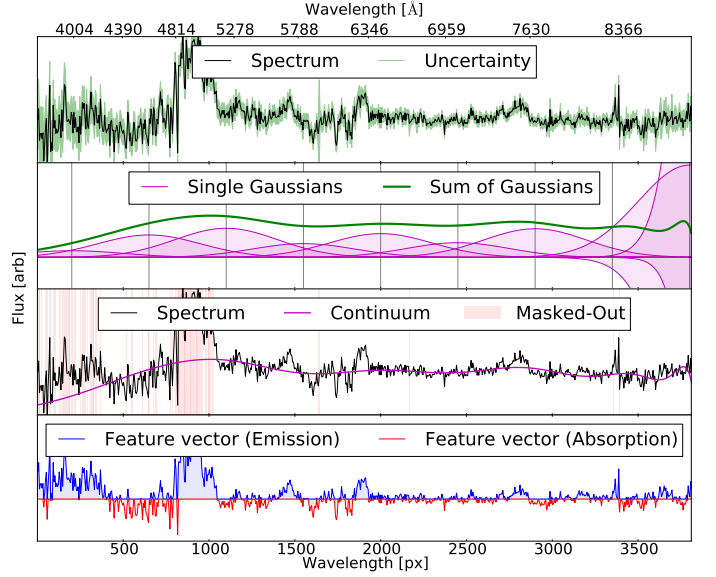
3.3.2. Continuum Estimation

The determination of the continuum is a very tricky problem which is known to cause difficulties when performing it automatically. For this reason we are not using the traditional continuum estimates (e.g. spline fitting, local weighting of polynomials²) and use a new hybrid method consisting of the following three approaches:

- fit multiple Gauss model to the data

² e.g. *onedspec*-package in the Image Reduction and Analysis Facility (IRAF) software package or *norm.pro* from the Interactive Data Language (IDL) software

Figure 2: *Top: Spectrum with uncertainty. Upper center: Decomposed continuum representation by Gaussians. Lower center: Spectrum with continuum fit and masked regions (ignored when fitting the continuum). Bottom: The extracted feature vectors are solely all pixel values with a value above/below zero for emission/absorption, all other values are set to zero.*



- weight penalty function with variance
- iterate 3 times, perform κ -clipping

In order to save computation time we follow the approach by Gieseke (2011) and use a multiple Gauss decomposition via gradient based optimization. This minimizes the risk of over- or underestimating the continuum flux as well as over-fitting which can be encountered when applying spline fits. In order to fit the continuum a number of n normalized Gaussians with the same width w [px] are placed on the dispersion axis with the first Gaussian being placed with an offset ω [px] and all following with a spacing of d [px]. The intensity of every individual Gaussian is a free parameter to be fitted. In comparison to polynomial and spline fitting the decomposition is less sensitive to individual spectral features and the computational effort is significantly lower. An illustration of the decomposition is shown in Figure 2. Based on the initial fit which is weighted with respect to the uncertainty $ivar$ (see 3.3.3), the root-mean-square is computed. Afterwards pixel values where the difference between fit and model exceeds $\kappa \cdot RMS$ are masked out for all future iterations of the continuum estimation. This is helpful to exclude large-scale deviations and to account for detector or night-sky artifacts.

Adjacently the spectrum is now normalized with respect to the estimated continuum C by a simple min-max-normalization:

$$\text{Flux}_{\text{norm}} = \frac{\text{Flux}_{\text{raw}} - \min(C)}{\max(C) - \min(C)} \quad (5)$$

such that the continuum of the normalized flux is located between 0 and 1 and the features are normalized with respect to continuum. As only the features are of interest for the following task the continuum is subtracted such that a flat spectrum is obtained. While testing different pre-processing parameters it turned out that the quality of the overall redshift is only marginally depending on the parameters used for estimating the continuum. An overview of the parameters and their impact on

Table 1: Parameters used in pre-processing with tested value range and impact on the outcoming distribution as well as on the time effort for the pre-processing.

	parameter description	range [used value]	impact [result / time]
n	number of Gaussians	8 - 20 [12]	low / linear
d	spacing between centers	300-700 [450]	low / none
ω	initial center offset of first Gaussian	100 - 400 [200]	none / none
w	Gaussian width	100 - 1,000 [300]	low / none
i	number of iterations for sigma clipping	1 - 3 [3]	none / linear
κ	noise deviation for feature refitting	0.1 - 3 [0.3]	low / none

computation time and the quality is given in table 1. **In contrast to the literature we treat the Ca-break also as a feature and thus if the continuum behaves smoothly around the break it can be seen as two close by absorption lines afterwards.**

3.3.3. Uncertainties

The SDSS spectra are affected by several uncertainties originating from the night sky, detector deficiency and read-out noise which are quantified pixel-wise by the inverse variance $ivar$ which corresponds to the noise uncertainty σ given by

$$\sigma = \frac{1}{\sqrt{ivar}} \quad (6)$$

After re-normalizing $ivar$ with respect to the continuum as described above, the extracted signal-to-continuum spectra are divided by 3σ in order to normalize the noise to values between -1 and 1, those will be called normalized S/N spectra (NSN-spectra hereafter). As a consequence the contrast between real signals and noise is further increased and artifacts originating from a bad sky subtraction/bad pixel are heavily suppressed.

3.4. Feature extraction

To extract the feature vectors we split the spectra into positive and negative flux components with respect to the fitted continuum (see bottom plot in Fig. 2). Thereby we create two feature vectors per spectrum. This simplification allows to keep the entire redshift-dependent information while no longer being dependent on the continuum shape. The separation enables us to compute individual redshifts for absorption and emission. By extracting subregions of this feature vector we can even obtain redshift information on single spectral regions. All values above the continuum (>0) are included in the feature vector for emission, all values below the continuum are simply set to zero, the same holds for absorption, vice-versa. Those extracted vectors are the input for our k NN-search described in Eq.3.

4. Experiments

We conducted two experiments with a different selection of features and a different reference sample, respectively. In the following they will be named Experiment 1 and 2.

4.1. Description of experiments

Both runs have been done on the full set of NSN-spectra. For the first experiment we applied the algorithm to the entire spectra and just discriminated between absorption/emission. In the second experiment we limited the dimensionality of the feature vector by just comparing specific spectral regions where features are expected for the redshift given by SDSS.

Naively one would expect a high precision in the former method as the full information content is available and thus the confusion between features of different origin (e.g. misidentifying H_β as H_α) should be fairly low. Other emission/absorption signature are available to cross-validate the redshift and hence minimize the probability of confusion. On the other hand the obtained global regression value is just valid for the entire spectrum and thus generalizes the information content too heavily.

For this reason a second experiment was conducted with a comparison restricted to single regions where prominent emission/absorption signatures are expected. It is worth noting that this experiment is tailored for detecting shifts of individual spectral lines. Additionally the methodology can be easily extended to allow a clustering/classification of the individual lines. We assume that the redshift of SDSS is correct for the entire spectrum but we search for redshift deviations of individual components. Since confusion will have a significant impact on the determination of the redshift we restrict the redshift deviation of the reference sample to a spectral window W defined by

$$W = \lambda_1 - \lambda_0 = (1 + z_{\text{high}}) \cdot \lambda_{\text{high}} - (1 + z_{\text{low}}) \cdot \lambda_{\text{low}} \quad (7)$$

with

$$\begin{aligned} z_{\text{low}} &= z_{\text{target}} - f \cdot (1 + z_{\text{target}}) \\ z_{\text{high}} &= z_{\text{target}} + f \cdot (1 + z_{\text{target}}) \end{aligned} \quad (8)$$

where f is the allowed deviation from the SDSS redshift (z_{target}) in units of the speed of light. A list of the spectral regions that have been taken into account can be found in Table 2. This list contains lines which are usually strong in star-forming/bursting galaxies and QSOs. The free parameter f influences the computational efforts, the chance of confusion (improving for small f) and the sensitivity to outliers where huge redshift deviations were achieved with large f , respectively. Throughout this paper we will use a value of $f = 0.05$. The big disadvantage of the second experiment is that confusion becomes a major issue. Especially for the entire data set it might be wise not to compare spectra to spectra of any redshift as it is likely that, e.g. the H_β ($\lambda 4861$) line can look similar to the [OIII] ($\lambda 5007$) line, see Fig.3, which obviously would lead to a wrong regression value. The benefit of this concept is its huge flexibility. Redshifts can now be computed for individual regions independently and thereby shifts can be detected. A more detailed discussion of the trade-off of confusion and multi-region regression value determination is given in Section 5.

4.2. Maximum deviation limit

One of the prerequisites in using the k NN approach was that a clear separation between noise and signal can be made. In principle there are two ways to reject spectra with no signal, the pre- and the post-selection. To pre-select one assumes that a signal has a certain shape and exceeds a given S/N limit. This can be simplified further to a measure which compares the average of a spectral region with a nominal value. As this pre-selection requires detailed knowledge about the shape/size/symmetry of

Figure 3: Cut-out of the same spectral region for 3 spectra with different redshift. If just this part is available the H_β line is indistinguishable from any of the two [OIII]-lines.

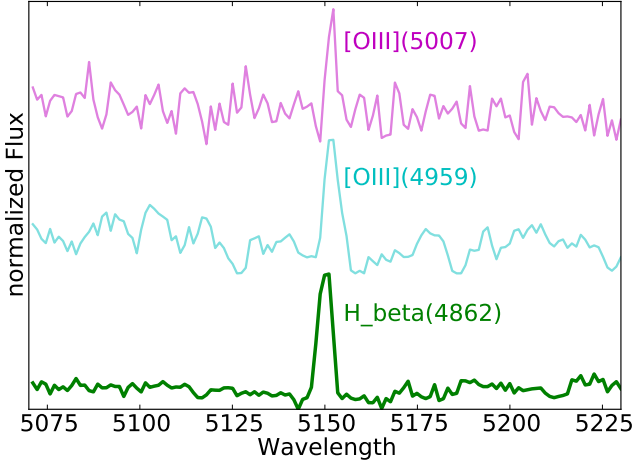


Table 2: List of regions taken into account.

Spectral type	λ_{low} [Å]	λ_{high} [Å]	Name
Emission	2,799	2,799	MgII
	3,346	3,426	NeV
	3,727	3,729	[OII]
	3,798	3,835	H ϵ , H ζ
	4,102	4,102	H δ
	4,341	4,363	H γ
	4,861	5,007	H β , [OIII]
	6,550	6,584	H α , [NII]
Absorption	6,716	6,731	[SII]
	3,934	3,969	H+K
	5,173	5,173	Mgb
	5,890	5,896	NaD

spectral features physical knowledge about the morphology of lines is required. In order to be independent of physical assumptions³ the possibility of a post-selection is chosen. The selected concept assumes that the deviation of the redshifts of the nearest neighbors over all targets follows a smooth distribution. For this distribution an upper limit can be (freely) selected which separates redshift estimates into good and noisy ones. This maximum deviation limit will be abbreviated by MDL.

An even bigger advantage of this method is that it allows to experiment with this free parameter in the evaluation stage, such that the k NN search is not performed for every individual value of MDL.

4.3. Validation strategy

In order to avoid biases in the regression values and when tuning the parameters the leave-one-out strategy is used. This means that the closest object (which is always the object itself) is not used for determining the redshift.

The fundamental assumption that most SDSS redshifts are correct was already discussed in subsection 3.2. Assuming now that all redshifts are correct we can compute something like a

³ Obviously the reference values by SDSS are obtained via physical modelling.

completeness, a correctness and a sensitivity. The completeness is a quite straightforward measure. It is the fraction of objects for which a redshift could be determined within the respective acceptance limit. In contrast to that the correctness is the fraction of objects where the computed and the SDSS redshift agree within their errors. Finally the sensitivity gives the reliability of all redshifts, i.e. it gives the typical deviation from the redshift. Therefore the standard deviation of the difference between SDSS and computed redshift of all valid spectral features is computed.

4.4. Parameter tuning

Despite the parameters described in the pre-processing step only two parameters have to be fine-tuned for the regression step⁴. Those are the number of k nearest neighbors used for the comparison and the MDL which marks a spectrum to be reliable. With the test strategy described in the previous section, this fine-tuning can be solved on a discrete grid, see Figure 4. In this plot two separate things are shown, the large scale behavior of the properties on the right side and on the left side a zoom-in to the lowest values of the MDL.

With increasing MDL, which is equal to accepting more noisy spectral features, the properties behave just as expected; while the completeness is increasing, the sensitivity and correctness of the model are decreasing. One can further see that the completeness is a rather flat function up to a MDL of 0.08 where it starts a more rapid, step-wise increase. The regression model breaks already down at a MDL of 0.05 where the sensitivity and correctness show a steep decrease. As the increase of the completeness is only very tiny for large values of MDL, we now focus on the region of very tiny values of MDL.

On the small scale the completeness strongly depends on the choice of the MDL and slight increases of the MDL yield a strong increase in completeness. Then the behavior becomes very flat and thus the gain by further increasing the MDL is only marginal (when increasing the MDL 5 times, the completeness fraction increases by less than 2%). It is worth noting that the completeness depends quite heavily on k . Smaller k values result in a more complete regression model. This indicates that the number of good references is of the order of 10-20 as for larger k values apparently more deviation is introduced in the regression model.

The sensitivity of the regression model is only decreasing in the beginning and follows then a fairly flat behavior with a slightly decreasing tendency. The dependence on the number of used neighbors is only marginal, though one can see that emission is in favor of a low k (little number of reference objects), while the sensitivity of the redshift in absorption is slightly better for higher values of k .

In the end the fraction of outliers on the good regression side is only slightly changing with increasing MDL and k . The decrease over the entire tested range is of the order of 0.5%.

The flat increase in completeness for MDL values larger than 0.001 allows us to minimize the effects on the sensitivity and correctness. We analyzed the impact of the choice of k on the different testing properties as well. The behavior of those with a fixed value of MDL of ≈ 0.0015 can be seen in Figure 5. An increasing number of nearest neighbors improves the sensitivity at the cost of a lower completeness. Thus as for the MDL the

⁴ Note that this is only partially true because different ways of computing the redshift and calculating the deviation exist. Besides the parameter tuning one has to choose a similarity measure and pre-process and select the features, accordingly.

Figure 4: Normalized completeness, sensitivity and correctness tested against different values of k and MDL. MDL is chosen to be 0.0015 as marked.

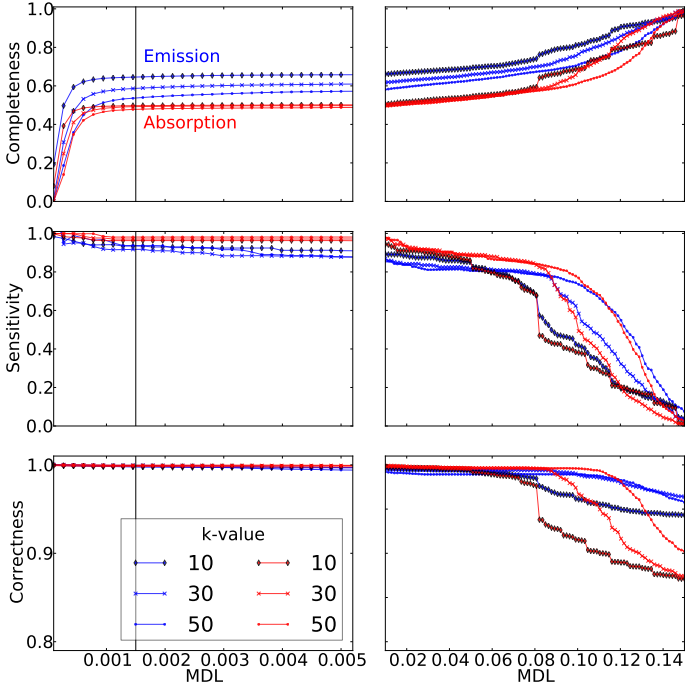
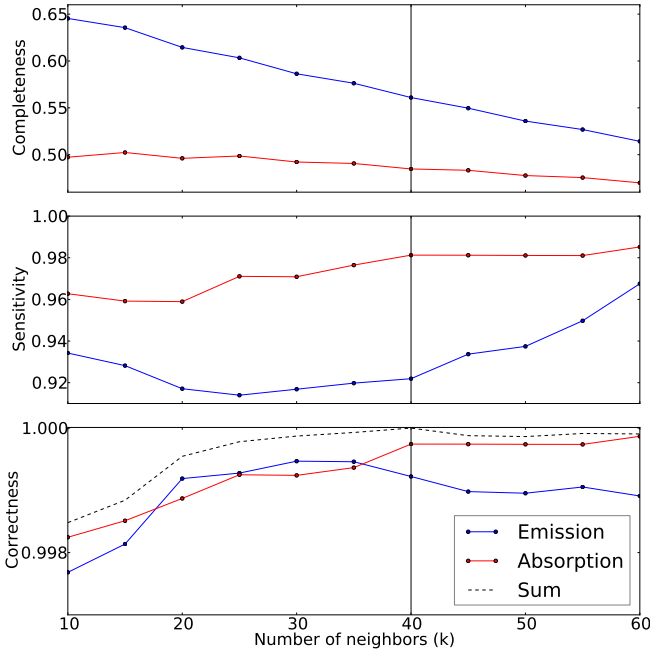


Figure 5: Dependence of test properties on k . For this plot MDL is fixed to 0.0015. k is chosen to be 40 as marked.



choice of k depends strongly on the desired completeness and precision.

4.5. Computational efforts

Applying the method described above to the test set is already quite time consuming on a single machine. It is evident that the

computational effort for 3 Million spectra is multiple times larger than with 16,000, i.e. the time complexity of a brute force k NN search scales with $O(n^2)$, thus the calculation time would already be of the order of years on a single machine. For future surveys this number will increase even faster such that more efficient approaches have to be found to resolve that problem. To speed up the calculation we parallelized the computation of the distances. The results presented here should solely give an overview on what is possible with even the simplest methods when such a huge data amount is available.

It is worth noting, that an online nearest neighbor search of incoming data (streaming) with a spectral database of the size of SDSS ($\approx 3,000,000$ spectra) is computationally easily feasible on a modern laptop. Assuming that a new instrument (e.g. 4MOST, de Jong et al. 2012) will obtain 2,400 spectra simultaneously, the approximate comparison time is of the order of 40h/core using a standard Python implementation. Using a machine with a simple GPU and a C-implementation will yield a speed-up of at least 100 compared to the single-CPU machine and can evaluate such a huge amount of data (<30 min) in less than the typical exposure time. Fortunately the computation of the distances can be perfectly parallelized, hence the presented method is well suited for scaling to larger surveys on modern computer architecture.

As already stated the computational effort is also strongly depending on the number of reference objects used for comparison to and obviously that is one of the most important screws to tune in order to minimize computing time. On the other hand the impact of selection effects is minimized by increasing the number of reference objects which have to be chosen in the most unbiased manner.

5. Results

In the following we will use the median absolute deviation (MAD) as deviation measure, which is defined as

$$\text{MAD}_{\bar{v}} = \text{median} (|\bar{v} - \text{median}(\bar{v})|)$$

for a list of values \bar{v} . In the following we will always use the **normalized difference in redshift** which is defined as:

$$\Delta Z_{\text{norm}} = \frac{z_{\text{kNN}} - z_{\text{SDSS}}}{1 + z_{\text{SDSS}}}$$

which corresponds to the difference in velocity in terms of c in the rest-frame of the SDSS redshift. In Fig. 4 one can see the behavior of the completeness, sensitivity and correctness as a function of the MDL as well as for different k . The curves follow the expected behavior; decreasing MDL will yield a low completeness but therefore high-quality redshifts. In the middle is a plateau until the MDL exceeds ≈ 0.10 . Beyond this value the completeness starts to converge against 1 and the quality of the redshifts against 0. While for the value added catalog a high completeness is desirable under moderate loss of sensitivity, thus MDL=0.07 and $k = 10$ are chosen. This increases the fraction of objects with a reliable redshift either in emission or in absorption up to a total of 80%. With this choice of parameters we have still a better sensitivity than SDSS with a significantly lower value in completeness (in SDSS $\approx 96\%$ of the targets have NO redshift warning). As stated earlier the choice of the reference sample, especially at high redshifts, will increase this fraction of our method significantly, just when excluding spectra with $z > 0.25$ the completeness increases to $\approx 90\%$.

In the following we concentrate on the detection and verification of outliers using MDL= 0.015 and $k = 40$. With that

choice we have traded a high sensitivity for a lower completeness of $\geq 50\%$. This enables us to efficiently detect outliers which show a wrong or multiple redshift components. In the following the outlier detection for both experiments will be discussed in detail.

5.1. Experiment 1

When using the entire spectral range for computing the redshift, we can obtain redshifts for 56% (emission), 49% (absorption) of the spectra. In Figure 6 the evaluation of the achieved performance is presented. In the second row of each figure one can see the frequency of deviations for emission and absorption, respectively⁵. As expected there is an exponential drop-off and a underlying uniform contribution. The top figure shows respectively the relative deviation (in units of the speed of light) between the redshift by SDSS and the computed ones. For nearly all of the objects with prominent features this deviation is below 0.1% c which corresponds roughly to the SDSS resolution.

In emission one can see three groups of outliers, three points between a redshift of $0.2 \leq z \leq 0.3$ (G1, magenta background), a straight line in the lower right of the plot (G2, cyan background), and three points that significantly deviate from the expected redshift below a redshift of $z \leq 0.1$ (G3, blue dots). The cause for each of the outliers groups is different but anyway well understood. The members of G1 are affected by the lack of reference objects in a comparable redshift range ($z > 0.2$) which agrees perfectly with the distribution shown in Figure 1. Thus the nearest neighbors will all have a lower redshift, moving all of those points to this region in the plot. It is worth noting that naively one would expect all of those points to lie on a horizontal line as well as the deviation from the reference set should for all objects be the same. In fact it turned out that the lowest point in this group is a truly shifted object. G2 is actually a superposition of the problem just described and what was defined earlier as confusion. The confusion occurs since the relative shift in redshift of $\Delta Z_{\text{norm}} \approx -0.25$ corresponds roughly to the shifts between $H_\alpha - H_\beta$ ($\Delta Z_{\text{norm}} = 0.26$), $H_\alpha - [\text{OIII}]$ ($\Delta Z_{\text{norm}} = 0.24$), $[\text{NII}] - H_\beta$ ($\Delta Z_{\text{norm}} = 0.26$) and $[\text{NII}] - [\text{OIII}]$ ($\Delta Z_{\text{norm}} = 0.24$). In this case the spectra usually show strong emission in either H_β or $[\text{OIII}]$ which are then (due to missing references) misidentified as $[\text{NII}]$ or H_α . Finally spectra with real shifts are likely to be observed close to the horizontal green line. They are further discussed in Subsection 5.3. The behavior of the noisy features can be explained by another superposition of two effects. The first group of objects is the one where the relative deviation is fairly low over the entire redshift range. Those objects are the result of the choice of the MDL - their redshift is still very accurate but they were moved to the uncertain features. A large number of spectra can be described very nicely with the applied model. This indicates that the MDL was selected quite conservatively. The rest of the data points in this plot do not show any signal of an emission feature thus they are just a random selection of redshifts from the initial distribution shown in Figure 1. The distribution of redshifts is fairly well approximated by a Gaussian (mean=0.14 and standard deviation=0.10). The functional form (cf. blue background plot in upper row) is:

$$((0.14 \pm 0.1) - z_{\text{SDSS}}) / (1 + z_{\text{SDSS}}) \quad (9)$$

⁵ Note that the bin width is changing by a factor of 25 from the left to the right side. For this reason the frequency between the two plots is not directly comparable

In absorption two outliers could be detected which show some anomalies that are well described by the computed redshift. Even redshifts with high MAD are still fairly reliable, supporting the restrictive limit on the MDL. The precision in absorption is of the same order as the emission, one per mil in units of the speed of light. Obviously the chance of confusion is dramatically smaller than for the emission which is the consequence of the lower number of potential features. Typically in a regular galaxy only three strong absorption features can be observed.

5.2. Experiment 2

In contrast to the first experiment the number of potential nearest neighbors of a specific spectral region depends now strongly on the choice of the redshift bin and additionally on the likelihood of the respective feature appearing in a galaxy spectra. This makes it inevitable to discuss the chosen regions individually. To have still a good comparison of the redshifts between the different regions, the MDL is set to 0.0015. For the sake of completeness all the figures comparing the noisy and the good features are presented in the Appendix A. Without restricting the results any further the number of potential outliers increased drastically due to the problem of additional confusion with different spectral features as well as to the limited number of used reference objects. Thus in order to remain clear and minimize the effect of methodological artifacts the deviation/outlier constraint is not just tested for $k=40$ but for an entire list of nearest neighbors, namely $k=[5,10,20,30]$. If the MAD violates the MDL or if the computed redshift agrees in its tolerance with the SDSS redshift for any k , the object is not marked as an outlier. Additionally objects which have redshifts $z < 0.05$ or $z > 0.3$ are automatically excluded from the outlier detection algorithm as here the limited number of comparison objects introduces spurious redshifts. As the different regions are biased by different effects they are adjacently discussed in more detail.

In the following we discuss the individual spectral emission and absorption features. Additionally groups and individual outlying spectra are discussed. **Exemplarily extensive plots for two spectral features are shown in the Appendix A.1,A.2 for H_β and NaD respectively.**

5.2.1. Emission

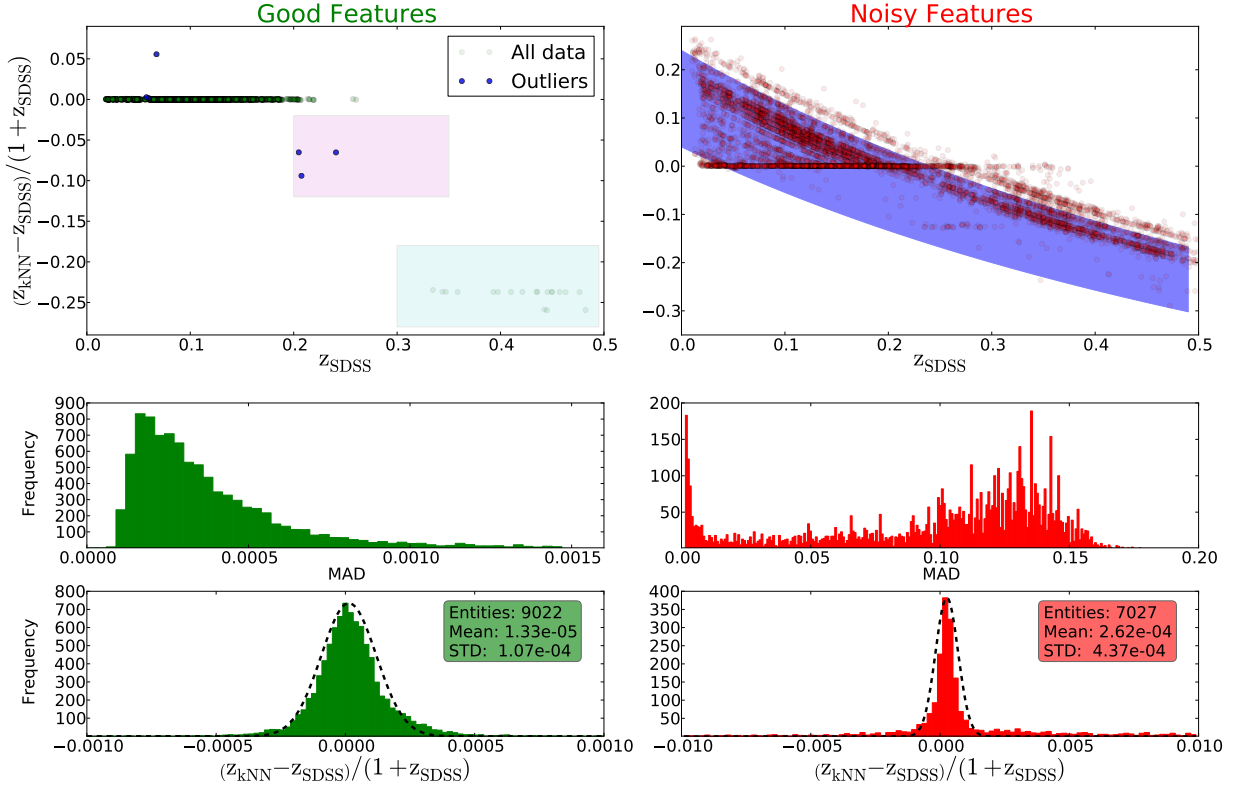
MgII, NeV ($\lambda 2,799, \lambda 3,346-3,426$) For those spectral regions a redshift of $z = 0.45/0.18$ is required to allow for a redshift determination. As the number density of objects is fairly sparse for such high redshifts and additionally the NeV feature does not occur in many of those spectra, none of the redshifts can be trusted.

[OII] ($\lambda 3,727-3,729$) This feature does not occur in all star-forming/active galaxies such that less than half of the redshifts could be trusted. Even in this small fraction of objects two outliers were detected which both show an actually shifted [OII]-line which is correctly described by the value determined by us.

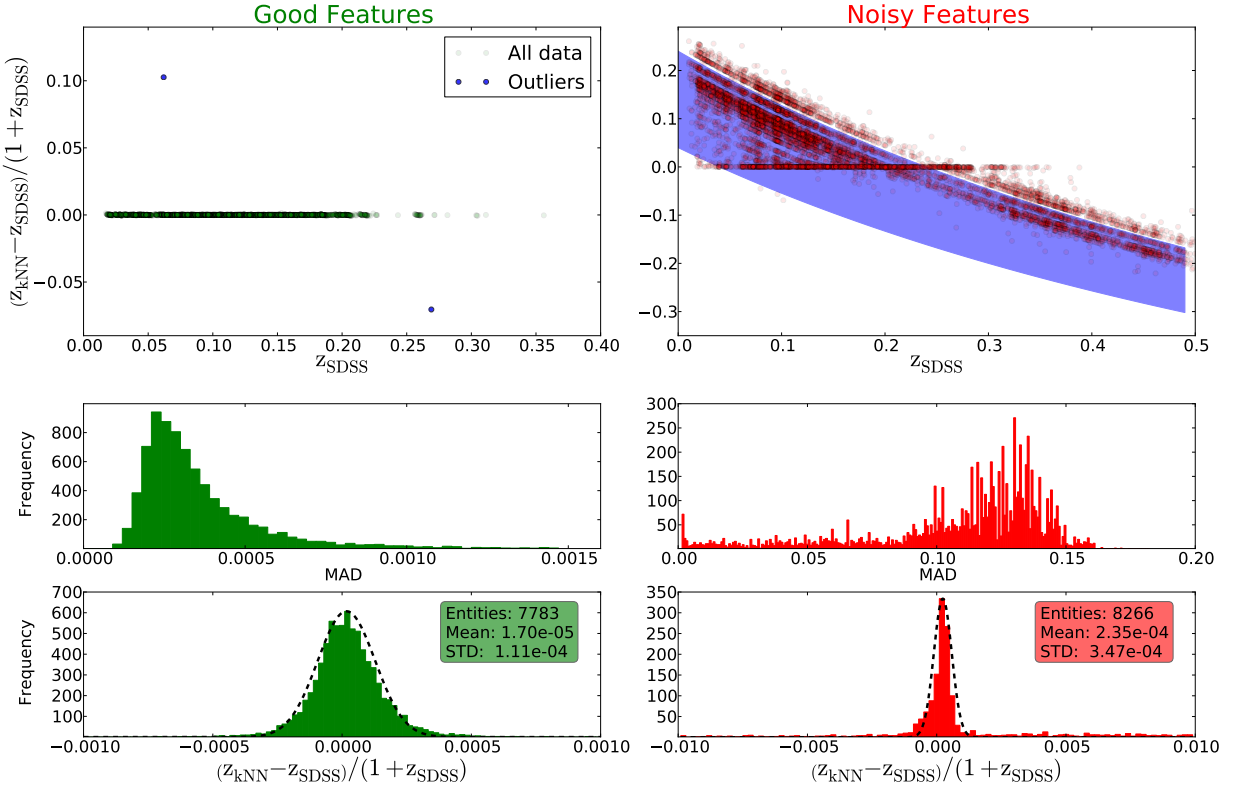
H_ϵ, H_ζ ($\lambda 3,798-3,835$) One of the objects found to have a shift in the [OII]-feature could be rediscovered. Both other additional spectral features are real.

H_δ ($\lambda 4,102$) This spectral feature just appears in emission for star-forming/bursting and active galaxies. The number of refer-

Figure 6: The evaluation of the performance for emission (a) and absorption (b): The relative deviation from the SDSS redshift as function of the SDSS redshift (top), the distribution of the MAD of the calculated redshift (middle) and the frequency of the relative deviation (bottom) are shown for the good (left) and the rejected noisy (right) spectral features, respectively. The blue background shade in the upper right figure reflects the objects which are entirely dominated by noise and thus their computed redshift just reflects a random draw of redshifts from the initial distribution, see Equation 9.



(a) Emission



(b) Absorption

ence objects exhibiting a clear sign of emission is fairly rare. In the corresponding plot one can see that two straight regions are apparent at $\Delta Z_{\text{norm}} = 0.04 / -0.04$ which are caused by confusion. The remaining object shows some very strong noise in the vicinity of the expected spectral feature.

$H_{\gamma}, [\text{OIII}]$ ($\lambda 4,342 - 4,363$) The only two remaining spectra have a $\Delta Z_{\text{norm}} = -0.032$. When investigating the origin of this shift, it appears that the shift is dominated by noise as the number of active and starburst objects (objects which possibly emit strong Balmer lines) in the specific redshift bins is very low (<5). So when selecting the redshift those few objects are strongly dominated by noise. Consequently this feature is not very reliable as long as not a representative reference sample can be selected.

$H_{\beta}, [\text{OIII}]$ ($\lambda 4,861-5,007$) In this spectral region the impact of confusion becomes dominant. 14 objects show a reasonably low deviation to be marked as good estimates. The horizontal line at $\Delta Z_{\text{norm}} = 0.03$ is caused by a misidentification of the red $[\text{OIII}]$ -line with the H_{β} -feature. The line at $\Delta Z_{\text{norm}} = 0.01$ is due to the confusion between the red and the blue $[\text{OIII}]$ -line. The negative confusion at $\Delta Z_{\text{norm}} = -0.03$ is the reverse effect of the first one. Another horizontal component at $\Delta Z_{\text{norm}} = -0.055$ is caused by a misidentification between the blue $[\text{OIII}]$ -line and HeII emission at $\lambda 4,685$.

Apart from all this confusion there is one regular shift which cannot be confirmed due to the lack of other emission features. The MAD for this object (0.0014) is close to the MDL so a lower choice of the MDL would tag this object as unreliable.

$H_{\alpha}, [\text{NII}]$ ($\lambda 6,550-6,584$) The outlier on the very top of the plot was already marked by the first run and is a truly shifted spectral feature. One of the shifts of the remaining two outliers is the result of an H_{α} -line in absorption and emission such that the red $[\text{NII}]$ -line was mistaken for it and in the other a very weak $[\text{NII}]$ emission line led to confusion with the H_{α} -line.

$[\text{SII}]$ ($\lambda 6,716-6,731$) The only object marked in the plot was also detected in the H_{α} -line as an outlier. It was already marked as an outlier in Experiment 1.

5.2.2. Absorption

Call (HK) ($\lambda 3,934-3,969$) All three targets highlighted as outlier are all truly shifted spectral features, one of them being the object already detected in emission (cf. Experiment 1).

Mgb ($\lambda 5,173$) Six of the objects are located on a horizontal line around $\Delta Z_{\text{norm}} = -0.06$. This corresponds to a misidentification of the Mgb absorption with the H_{β} in absorption. Indeed all highlighted objects show a very prominent H_{β} feature in absorption. Two of the remaining objects have a very strong absorption feature originating from deficient nightsky subtraction, not properly described by *ivar*. Three objects are active galaxies and show extremely strong emission features in this region. The number of active galaxies in the reference sample is not sufficient to reproduce this behavior. The remaining object shows a true shift in the Mgb line.

NaD ($\lambda 5,890-5,896$) For seven spectra a shift of the NaD could be confirmed by a manual inspection, for all the others a badly subtracted sky at around $\lambda 7,200$ was not described correctly by *ivar*, leading to a very prominent absorption feature which was mistaken for NaD.

5.3. Manually Investigated Objects

To validate the method a manual inspection of the outliers is mandatory. A spectrum was investigated if it was selected as an outlier in any of the spectral regions (from Experiment 1 and 2) and if it was not part of one of the horizontal lines introduced by confusion. The outliers have different origins which can be roughly classified into three groups: objects with real multiple redshift components (true), objects with detector/nightsky artifacts which were not properly described by *ivar* (fake) and objects where the redshift computation simply failed (wrong).

37 objects were eventually investigated manually, three of those have been marked by several features as outlier. 38% (14) of the outliers are spectra with truly shifted redshift components. In 11 of those the shift between the redshift components is lower than 10,000 km/s thus those components do certainly have a physical origin. The remaining three spectra of the true class are likely to be superpositions and/or lensed objects. The fake category contains 10 objects where a badly described detector/nightsky artifact was confused with NaD or Mgb absorption. It is impossible to exclude those objects previously as there is no unique position/indication of the existence of such a feature. The 13 spectra in the wrong class are mainly a result of a biased reference sample which additionally contains a low number of active and star-bursting galaxies. There is a good chance that the fraction of those objects can be significantly decreased if a more representative reference sample is used for the comparison.

A short summary of all manually investigated objects with identifier, SDSS and computed redshift can be found in Table A.1.

5.4. Most Prominent Outliers

The most prominent outliers will be shortly described here to emphasize the power of this outlier detection scheme. In Figure 7 one can see the three truly shifted objects with the highest velocity offset. While the first two (J094419.05-004051.44, J120419.07-001855.93) were tagged even independently by the separate runs, the last one (J113154.29+001719.02) did not show up in the second experiment as the relative shift between our computed and the SDSS redshift (0.077 c) exceeds the allowed range of the shift (0.060 c). In the first and last object the model applied by SDSS describes the absorption behavior quite well but the emission features are not described at all such that a second component with a strongly shifted redshift is needed to describe those. While they quite nicely demonstrate the power of the method these objects are astronomically less interesting. It is likely, due to missing signs of interaction, that those are just simple superpositions of objects. In the *i*-band of the first object a tiny and asymmetric arc (cf. Fig. 8) can be seen which could indicate a lensed object. The redshift of the second object was estimated entirely wrong by SDSS as apparently none of the template models was able to describe the continuum and the line behavior at the same time. The newly estimated redshift on the other hand describes the spectrum quite well. While the new fit does not support the existence of another component it is worth

Figure 7: The three most extreme outliers obtained from our regression model are shown. The green line in the background is the SDSS spectrum with the gray spectrum at the bottom being the typical noise deviation. The red curve shows the fitted spectrum with a redshift as obtained by SDSS, the blue curve is the overplotted spectrum with the redshift as obtained by our regression model.

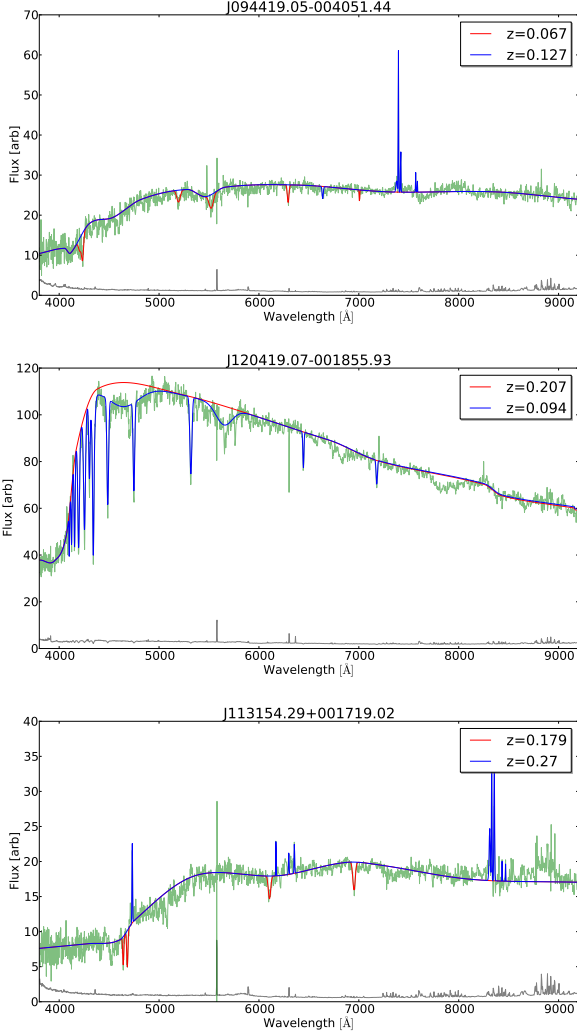
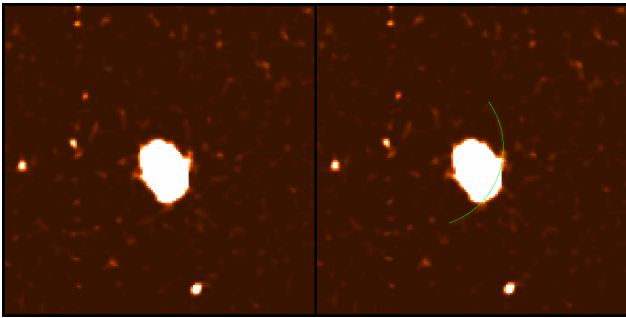


Figure 8: SDSS i -band image of J094419.05-004051.44 (smoothed with Gaussian blur of 3 pixel width). In the right image the asymmetric arc has been overplotted by a green circle.



noting that on the SDSS image a clear symmetric arc can be seen at a distance of a few arc-seconds.

5.5. Summary Of Outliers

In Table A all outliers found are summarized. Targets where a true feature exists are marked. The possible origins for the existence of multiple redshift components are miscellaneous. For a very high shift between the redshifts the most likely explanation is a chance superposition of two objects. If those are at an according distance to each other and to the observer an arc due to gravitational lensing might be observed. The number of gravitational lenses in the near universe is very limited so far (Muñoz et al. 1998). Spectra with the velocity shifts between the lines lower than $< 10,000$ km/s might be good candidates for being super-massive black hole binaries (SMBHB, Tsalmantza et al. 2011; Fu et al. 2012; Popović 2012). The kinematics of the broad line region are a very common cause for such observed line shifts as well (Shen et al. 2011).

Eventually one could only discriminate between the different origins by either deep-imaging (lenses) or by follow-up spectroscopy (SMBHB, Liu et al. 2014). High-resolution imaging in the multiple wavelengths could also distinguish single from multiple sources (e.g. Rodriguez et al. 2009).

6. Summary

This paper presents a new methodology which performs a redshift computation based on pre-existing SDSS redshifts. The aim is to obtain improved redshifts for emission and absorption as well as for individual spectral features. This enables astronomers to detect spectra with multiple redshift components. The basic principle of the presented method is to perform a self-consistency check such that objects which look similar should have a comparable redshift.

First of all, it is worth noting that this method performs quite well in calculating the redshift for very different kinds of spectra. The only requirement is that the density of reference objects is reasonably high in the d -dimensional Euclidean space populated by the spectra. It could be shown that this method with its current set of reference spectra (which is limited to redshifts $z \leq 0.5$, but the reference sample is just densely populated until $z \approx 0.2$) can reach a higher sensitivity than the SDSS pipeline for individual spectra. So far only the completeness is considerably lower than in the SDSS pipeline, but this will be improved via a larger and more representative reference sample which covers all redshifts.

To show the power of this new tool, in this work we presented outliers found in the data set. For this a more conservative (more sensitive, but less complete) parameter set has been chosen. We were able to detect outliers by two different statistical redshifts: The first approach focuses on the overall behavior of the spectra, thus being less affected by confusion but being less informative. The second approach is focusing on the behavior of predefined regions. Its completeness rate is higher, i.e. more objects with exotic behavior have been found. On the other hand the number of highlighted objects which appear due to methodological artifacts is also increased. In summary both methods yield very interesting objects where the SDSS redshift was wrong.

Even though these methods work quite nicely plenty of parameters exist which are tunable and have impact on the final result. In the data pre-processing several models describing the continuum behavior were investigated. The normalization of the spectra with respect to this continuum and their noise might have an effect on the number of true outliers, too. In addition the feature extraction has a severe impact on the final results and might be tailored to certain scientific needs.

6.1. Future Work

In a next step we will investigate the impact of the choice of the reference sample. Each redshift bin should contain enough reference objects to minimize systematical effects due to the bias of the sample. This discussion is part of a forthcoming paper where the methodology is applied to the full SDSS spectroscopic database.

In a final step the impact of the mathematical composition of the regression values used in Equation 3 could be investigated. It would further be interesting to study the behavior of different selection measure such that a clearer distinction between noisy and good features can be made. Additionally one could apply a pre- instead of a post-selection to distinguish between signals and noise on the data level. This would make the reduction of the reference sample in the computational step easier, as just reference objects with an existing signal would be used for comparison. On the other hand it would introduce further biases which have to be tuned by the increased number of parameters. Some physical knowledge about the type of signal which is expected would be required.

Finally the outlier detection could be modified. Depending on the scientific use case the trade-off between completeness and sensitivity can be adjusted by using different detection criteria. Those detected outliers can be related to in future outlier catalogs. As we are currently only investigating a small fraction of the database (<1%) a huge number of objects is expected to be marked as outliers for the entire dataset, i.e. that the number of objects to be investigated will be so large ($\approx 5,000$) that a manual inspection will be extremely time-consuming. Anyway the discovery potential of this straightforward redshift determination approach is huge. The applicability to compute model-independent redshifts of new incoming data was already shown on this simplified and just partially representative sub-sample.

Acknowledgements. Funding for SDSS-III has been provided by the Alfred P. Sloan Foundation, the Participating Institutions, the National Science Foundation, and the U.S. Department of Energy Office of Science. The SDSS-III web site is <http://www.sdss3.org/>. SDSS-III is managed by the Astrophysical Research Consortium for the Participating Institutions of the SDSS-III Collaboration including the University of Arizona, the Brazilian Participation Group, Brookhaven National Laboratory, Carnegie Mellon University, University of Florida, the French Participation Group, the German Participation Group, Harvard University, the Instituto de Astrofísica de Canarias, the Michigan State/Notre Dame/JINA Participation Group, Johns Hopkins University, Lawrence Berkeley National Laboratory, Max Planck Institute for Astrophysics, Max Planck Institute for Extraterrestrial Physics, New Mexico State University, New York University, Ohio State University, Pennsylvania State University, University of Portsmouth, Princeton University, the Spanish Participation Group, University of Tokyo, University of Utah, Vanderbilt University, University of Virginia, University of Washington, and Yale University.

The authors thank Michael Schick for very fruitful discussions on the topic of uncertainty quantification. SDK would like to thank the Klaus Tschira Foundation for their financial support.

References

- Ahn, C. P., Alexandroff, R., Allende Prieto, C., et al. 2014, *ApJS*, 211, 17
 Ball, N. M. & Brunner, R. J. 2010, *International Journal of Modern Physics D*, 19, 1049
 Bellman, R. & Bellman, R. E. 1961, *Adaptive Control Processes: A Guided Tour*. (Princeton University Press)
 Bolton, A. S., Burles, S., Schlegel, D. J., Eisenstein, D. J., & Brinkmann, J. 2004, *AJ*, 127, 1860
 Bolton, A. S., Schlegel, D. J., Aubourg, É., et al. 2012, *AJ*, 144, 144
 Borne, K. 2009, *ArXiv e-prints*
 Cui, X.-Q., Zhao, Y.-H., Chu, Y.-Q., et al. 2012, *Research in Astronomy and Astrophysics*, 12, 1197

- de Jong, R. S., Bellido-Tirado, O., Chiappini, C., et al. 2012, in *Society of Photo-Optical Instrumentation Engineers (SPIE) Conference Series*, Vol. 8446, Society of Photo-Optical Instrumentation Engineers (SPIE) Conference Series
 Eisenstein, D. J., Annis, J., Gunn, J. E., et al. 2001, *AJ*, 122, 2267
 Fu, H., Yan, L., Myers, A. D., et al. 2012, *ApJ*, 745, 67
 Gieseke, F. 2011, dissertation, Universität Oldenburg
 Gieseke, F., Polsterer, K. L., Thom, A., et al. 2011, *ArXiv e-prints*
 Hastie, T., Tibshirani, R., & Friedman, J. 2009, *The Elements of Statistical Learning: Data Mining, Inference, and Prediction*. (Springer), second Edition
 Laurino, O., D'Abrusco, R., Longo, G., & Riccio, G. 2011, *MNRAS*, 418, 2165
 Liu, X., Shen, Y., Bian, F., Loeb, A., & Tremaine, S. 2014, *ApJ*, 789, 140
 Meusinger, H., Schalldach, P., Scholz, R.-D., et al. 2012, *A&A*, 541, A77
 Muñoz, J. A., Falco, E. E., Kochanek, C. S., et al. 1998, *Ap&SS*, 263, 51
 Polsterer, K. L., Zinn, P.-C., & Gieseke, F. 2013, *MNRAS*, 428, 226
 Popović, L. Č. 2012, *New Astronomy Reviews*, 56, 74
 Richards, G. T., Fan, X., Newberg, H. J., et al. 2002, *AJ*, 123, 2945
 Richards, J. W., Freeman, P. E., Lee, A. B., & Schafer, C. M. 2009, *ApJ*, 691, 32
 Rodriguez, C., Taylor, G. B., Zavala, R. T., Pihlström, Y. M., & Peck, A. B. 2009, *ApJ*, 697, 37
 Shen, Y., Richards, G. T., Strauss, M. A., et al. 2011, *ApJS*, 194, 45
 Strauss, M. A., Weinberg, D. H., Lupton, R. H., et al. 2002, *AJ*, 124, 1810
 Tsalmantza, P., Decarli, R., Dotti, M., & Hogg, D. W. 2011, *ApJ*, 738, 20
 York, D. G., Adelman, J., Anderson, Jr., J. E., et al. 2000, *AJ*, 120, 1579

Appendix A: Appendix

Table A.1: Summary of all manually investigated spectra. The spectral features *Em*, *Abs* are from Experiment 1, all others mark the respective regions where the feature was detected as an outlier. Sorting is by number of spectral features, spectral feature and finally identifier.

Identifier [plate-MJD-fiber]	z_{SDSS}	z_{EST}	Δz [km/s]	Spectral Feature	Class	Remarks
0266-51602-0095	0.0673	0.1266±0.0005	16600	Em,H α ,[NII],[SII]	true	Fig. 7 top
0286-51999-0236	0.2075	0.0940±0.0007	-28200	Em,CaII,NaD	true	possible lense, Fig. 7 center
0268-51633-0423	0.1699	0.1689±0.0005	-300	OII,H ϵ ,H ζ	true	shifted BL/NL
0275-51910-0265	0.0596	0.0614±0.0013	500	Em	wrong	low number density of reference objects (see Fig. 1)
0279-51984-0449	0.2049	0.1264±0.0014	-19600	Em	wrong	member of G1
0280-51612-0323	0.0576	0.0605±0.0007	800	Em	wrong	low number density of reference objects (see Fig. 1)
0282-51658-0493	0.2409	0.1600±0.0009	-19600	Em	wrong	member of G1
0267-51608-0601	0.0620	0.1709±0.0006	30700	Abs	fake	fake feature at $\lambda 6, 901$
0282-51630-0400	0.2690	0.1796±0.0008	-21200	Abs	true	Fig. 7 bottom
0274-51913-0617	0.0966	0.1159±0.0004	5200	OII	true	dual core in image
0272-51941-0332	0.2201	0.2184±0.0010	-500	H ϵ ,H ζ	true	NL shifted vs. absorption
0288-52000-0215	0.1531	0.1543±0.0007	200	H ϵ ,H ζ	true	shifted BL/NL
0268-51633-0354	0.0918	0.0928±0.0006	200	H δ	wrong	strong noise in spectral region
0271-51883-0371	0.1202	0.0851±0.0012	-9500	H γ	wrong	litte active & starburst spectra
0273-51957-0579	0.1312	0.0946±0.0007	-9800	H γ	wrong	litte active & starburst spectra
0279-51608-0034	0.1010	0.0975±0.0014	-1000	H β ,[OIII]	wrong	high MAD
0271-51883-0570	0.0531	0.0638±0.0013	3000	H α ,[NII]	wrong	low number density of reference objects (see Fig. 1)
0286-51999-0089	0.1296	0.1263±0.0004	-900	H α ,[NII]	wrong	very weak features only
0267-51608-0593	0.1631	0.1642±0.0005	200	CaII	true	
0275-51910-0142	0.1516	0.1526±0.0005	200	CaII	true	
0266-51602-0604	0.2995	0.3353±0.0012	8200	Mgb	fake	$\lambda 6, 913$
0266-51630-0374	0.1661	0.1449±0.0007	-5500	Mgb	fake	$\lambda 5, 892$
0270-51909-0537	0.1774	0.1589±0.0010	-4800	Mgb	wrong	QSO, sparse in reference
0277-51908-0277	0.2822	0.2593±0.0013	-5400	Mgb	wrong	QSO, sparse in reference
0285-51930-0170	0.1794	0.1685±0.0009	-2800	Mgb	wrong	QSO, sparse in reference
0288-52000-0215	0.1531	0.1544±0.0006	300	Mgb	true	shifted BL/NL
0266-51630-0318	0.1483	0.1706±0.0008	5800	NaD	fake	$\lambda 6, 901$
0267-51608-0092	0.1467	0.1456±0.0005	-300	NaD	true	only NaD shifted
0267-51608-0320	0.1164	0.1836±0.0010	18000	NaD	fake	$\lambda 6, 976$
0269-51910-0531	0.1278	0.1958±0.0011	18000	NaD	fake	$\lambda 7, 045$
0270-51909-0114	0.1970	0.1960±0.0007	-300	NaD	true	only NaD shifted
0274-51913-0548	0.1000	0.0979±0.0002	-600	NaD	true	only NaD shifted
0283-51660-0602	0.1281	0.1968±0.0007	18200	NaD	fake	$\lambda 7, 053$
0284-51943-0531	0.1578	0.1958±0.0005	9800	NaD	fake	$\lambda 7, 048$
0284-51943-0603	0.2013	0.1985±0.0006	-700	NaD	fake	$\lambda 7, 062$
0285-51663-0602	0.2426	0.1979±0.0007	-10800	NaD	fake	$\lambda 7, 058$
0285-51930-0035	0.1222	0.1212±0.0002	-300	NaD	true	only NaD shifted

Figure A.1: The analysis of the $H\beta, [OIII]$ region is shown. One can see the relative difference in redshift against the SDSS redshift (top), the distribution of the deviations (middle) and a histogram of the relative difference in redshift (bottom). Noisy spectral features are marked in red, good features in green.

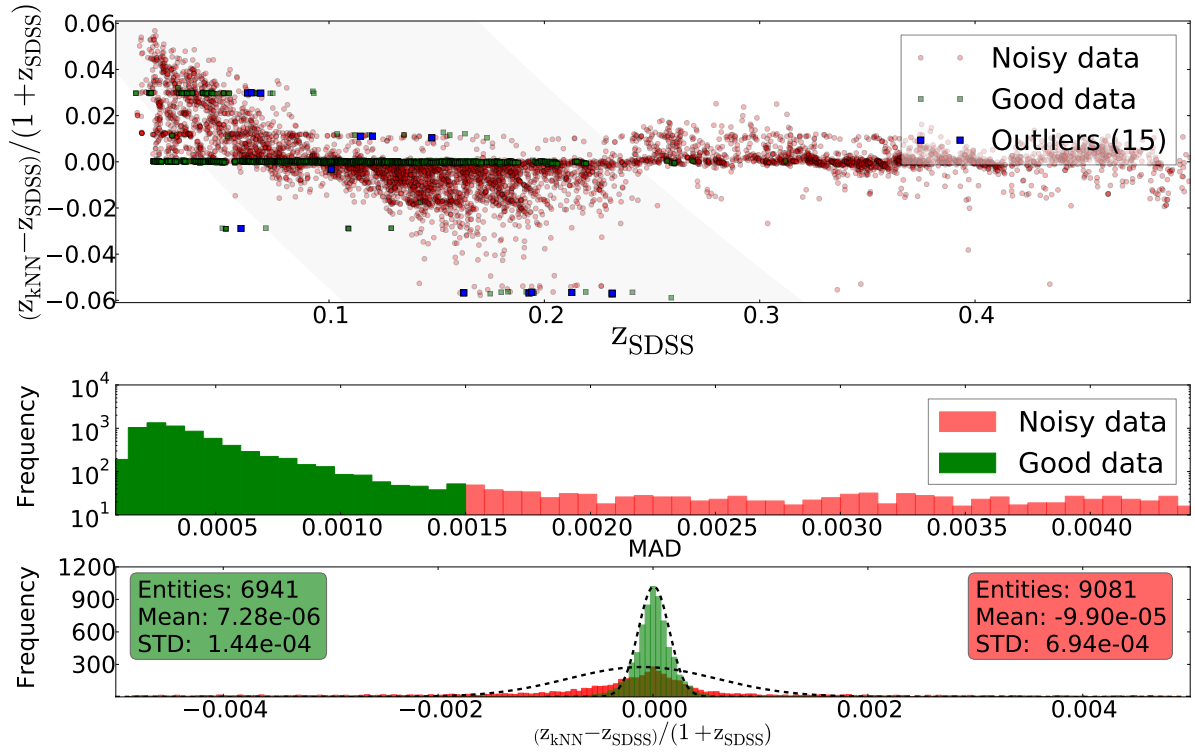


Figure A.2: The analysis of the NaD region is shown. One can see the relative difference in redshift against the SDSS redshift (top), the distribution of the deviations (middle) and a histogram of the relative difference in redshift (bottom). Noisy spectral features are marked in red, good features in green.

